

Widespread and systematic effects of fire on plant–soil water relations

Received: 8 September 2023

Accepted: 16 September 2024

Published online: 7 November 2024

Martin J. Baur^{1,2}✉, Andrew D. Friend^{1,2} & Adam F. A. Pellegrini^{1,2,3}

Wildfire activity and the hydrological cycle are strongly interlinked. While it is well known that wildfire occurrence and intensity are controlled by water availability, less is known about the effects of wildfire on plant and soil water cycling, especially at large scales. Here we investigate this by analysing fire impacts on the coupling between plant and soil water content, at the global scale, using remote sensing of soil moisture, vegetation water content and burned area. We find a strong effect of fire on plant–soil water relations, accelerating soil moisture loss by 17% and leading to faster gains in vegetation water content by 62%, both of which are positively related to fire severity and largest in forests. This effect is spatially extensive, with accelerated soil moisture loss found in 67%, and increased vegetation water content gain found in 67% of all analysed burned areas. After fire, plants also tended to have less control on their water content (that is, were more anisohydric). In summary, fire changes ecosystem functioning by increasing ecosystem water losses and shifting the relationship between soil and vegetation water budgets. With climate change, wildfire is likely to play an increasingly important role in ecosystem water cycling and subsequent ecosystem recovery.

Plants primarily acquire water from the soil, leading to a strong coupling between soil moisture (SM) and vegetation water content (VWC)^{1,2}, often referred to as plant–soil water relations. Plant–soil water relations are fundamental to understanding water transport in the soil plant atmosphere continuum and the effects of water availability on plant productivity^{3,4}. As plant transpiration contributes substantially to the global flux of water between the land and atmosphere^{5,6}, plant–soil water relations play a substantial role in the carbon, water and energy cycles. In fact, the responses of SM and VWC to water pulses and their coupled dynamics during soil drying can be indicative of plant hydraulic strategies and water stress^{7,8}. Plant–soil water relations are not constant in space and time⁷ but can be changed by ecosystem disturbances, such as large-scale fires⁹. Fire can change SM and VWC dynamics by removing vegetation biomass, altering vegetation composition and triggering regeneration mechanisms.

However, the generality, extent and magnitude of fire effects on plant–soil water relations as well as their modifying factors are unknown, limiting our ability to predict the responses of the water cycle and ecosystems to fire events, which might become more frequent and severe with global change^{10,11}.

As wildfire occurrence is limited by fuel load and fuel moisture^{12,13}, fires are often preceded by positive VWC, indicative of a high fuel load, and negative SM, indicative of low moisture, anomalies, which are more likely to occur during the dry season¹⁴. After fires, the VWC is lower due to the burning and continued drying of the vegetation. Consequently, observed fire effects on local hydrology, such as changed evapotranspiration^{15,16} and increased overland flow^{17,18}, often resulting in altered watershed discharge¹⁹, could arise from either changes in SM and VWC state independently, or through a modification of the interactions between SM and VWC (that is, plant–soil water relations). The relative roles of SM, VWC and their interactions remain unclear, as most previous studies compare pre- and post-fire conditions without separating effects caused by changes in SM and VWC state from effects caused by changes in plant–soil water relations. Furthermore, it is not known whether potential changes in plant–soil water relations are substantial on large scales and whether they occur consistently across different ecosystems. The vast extent of, and limited accessibility to, burned areas, as well as the time intensity and difficulty of taking field-based measurements of SM and VWC in fire-affected

¹Department of Geography, University of Cambridge, Cambridge, UK. ²Conservation Research Institute, University of Cambridge, Cambridge, UK.³Department of Plant Sciences, University of Cambridge, Cambridge, UK. ✉e-mail: mjb311@cam.ac.uk

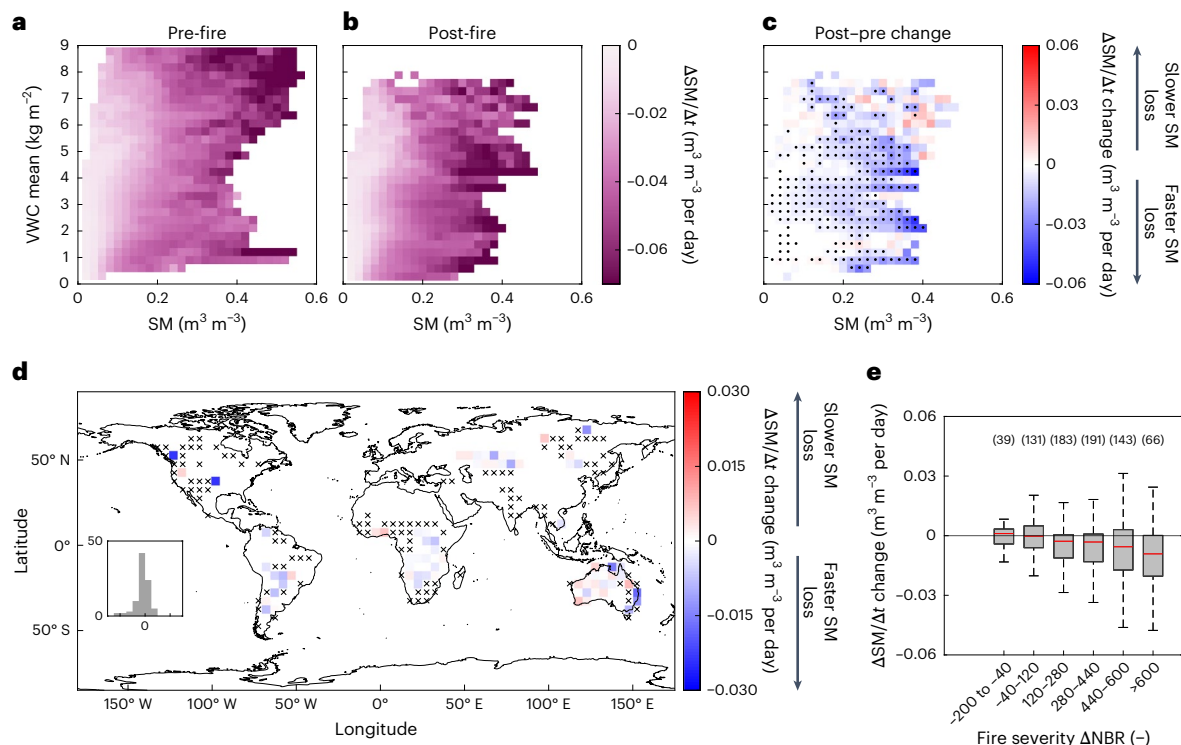


Fig. 1 | Fire changes the SM loss rate, $\frac{\Delta SM}{\Delta t}$, across SM and VWC conditions. **a–c**, Median pre-fire $\frac{\Delta SM}{\Delta t}$ (**a**), median post-fire $\frac{\Delta SM}{\Delta t}$ (**b**) and post- minus pre-fire difference (**c**). We use a two-sided Wilcoxon rank sum test to determine if pre- and post-fire samples come from continuous distributions of equal mean. If this is rejected at a 5% significance level, tiles in **c** are stippled. SM and VWC conditions with fewer than 20 samples are not shown. **d**, A map of the median difference

between post- and pre-fire $\frac{\Delta SM}{\Delta t}$ binned into a 5° grid, SM and VWC conditions with fewer than ten samples are excluded. Areas with all conditions below this threshold are indicated by crosses. **e**, $\frac{\Delta SM}{\Delta t}$ change relative to ΔNBR fire severity. The boxplots display median and 25th and 75th percentile of the distribution. The whiskers include approximately 99.3% of all datapoints, and outliers are not displayed.

areas, necessitates the use of remote sensing to assess fire effects on plant–soil water relations globally. We hypothesize that fire consistently impacts plant–soil water relations at large scales, subsequently changing post-fire SM and VWC dynamics and leading to altered plant water use strategies across ecosystems²⁰.

We use nearly 6 years (1 April 2015 to 31 December 2020) of SM and VWC microwave remote sensing observations to analyse plant–soil water relations across the global burned area. We use SM and VWC data from the Soil Moisture Active Passive (SMAP) mission and the Advanced Microwave Scanning Radiometer 2 (AMSR2) system. Both have high temporal revisits (a few days) and provide data at ca. 9 km resolution, which is also our study resolution. VWC is calculated from vegetation optical depth (VOD) (Methods). SM and VWC from microwave remote sensing are commonly used to measure water uptake by plants, understand drivers of SM loss²¹, assess post-fire recovery of vegetation^{22,23} and estimate plant isohydricity²⁴, a metric of how strongly plants control their water content. SM and VWC remote sensing retrievals become more uncertain with increasing vegetation, but this uncertainty is less critical in our study, given that we mostly analyse regions with sufficient penetration of the signal through the vegetation canopy, that is, with a VOD < 1. We combine SM and VWC observations with a global burn severity database (MOSEV)²⁵ to locate burned areas and compare post-fire plant–soil water relations to a pre-fire reference state, while considering fire severity using the delta normalized burn ratio (ΔNBR)^{26,27}. ΔNBR uses near-infrared channels to assess the change in surface properties before and after fire. Overall, 11,027 SMAP pixels burned during our study period, with 18% of them experiencing more than one fire event.

We isolate the effects of fire on plant–soil water relations by applying several steps to correct for systematic differences in climatic conditions pre- and post-fire, and investigate the role of atmospheric water

demand, namely, vapour pressure deficit (VPD) (Methods). To assess the responses of SM and VWC to fire, we use their mean rates of change, $\frac{\Delta SM}{\Delta t}$ and $\frac{\Delta VWC}{\Delta t}$. We assessed the responses of the rates of change across a phase space of SM and VWC conditions. This is important because the SM and VWC rates of changes depend on mean SM and VWC; for example, at high SM (saturated conditions) water loss is faster than at low SM (unsaturated conditions). This is consistent with the concept of water retention curves and observations^{28,29}.

SM loss is accelerated post-fire

To test how fires affect SM losses, we compared SM drydowns from the SMAP mission before and after fire events. A drydown is defined as a series of at least four consecutively decreasing SM observations. There is negligible precipitation during a drydown, meaning that the SM rate of change, or $\frac{\Delta SM}{\Delta t}$, is consistently negative because of net water losses (that is, from run-off, drainage and evapotranspiration)^{30,31}. We compute mean rates of change as finite differences over the sampled time period, for example, $(\frac{\Delta SM}{\Delta t} = SM_{t+1} - SM_t)$. By comparing 0–30 days post-fire with the same 30 days in the previous years, we avoid comparing across different seasons (Methods). As fire affects SM and VWC conditions, one main difference being that VWC is lower post-fire owing to the burning of vegetation, we binned pre- and post-fire $\frac{\Delta SM}{\Delta t}$ on the basis of SM and VWC conditions (Fig. 1a–c), therefore accounting for systematic differences between pre- and post-fire SM and VWC. This is important as SM loss progressively decreases in drying soils^{29,32}, due to the nonlinear decrease of the soil matric potential and soil conductivity with decreasing SM. In line with this, we find higher SM loss, that is, more negative $\frac{\Delta SM}{\Delta t}$, at higher SM (Fig. 1a,b). The median change between post- and pre-fire $\frac{\Delta SM}{\Delta t}$ is negative, changing $\frac{\Delta SM}{\Delta t}$ by a median value of −17%, which indicates more rapid post-fire SM

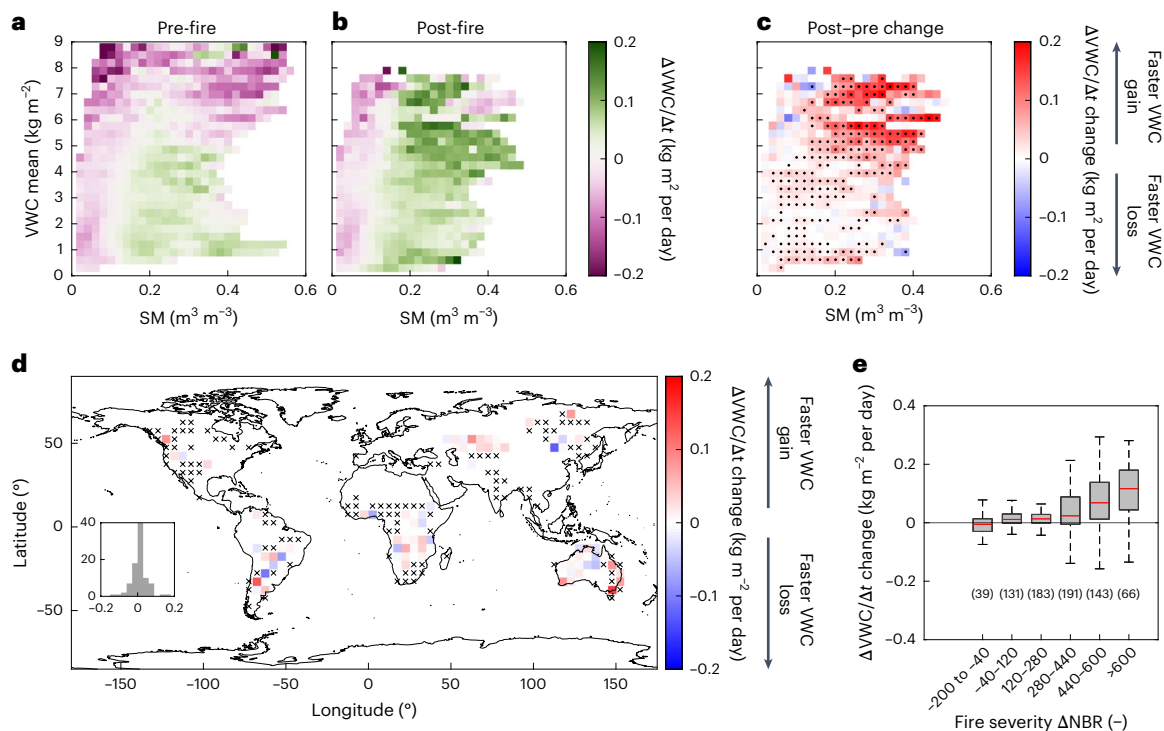


Fig. 2 | Global effects of fire on the VWC rate of change, $\frac{\Delta VWC}{\Delta t}$. **a–c**, Median pre-fire $\frac{\Delta VWC}{\Delta t}$ (**a**), median post-fire $\frac{\Delta VWC}{\Delta t}$ (**b**) and $\frac{\Delta VWC}{\Delta t}$ post- minus pre-fire difference (**c**). We use a two-sided Wilcoxon rank sum test to determine if pre- and post-fire samples come from continuous distributions of equal mean. If this is rejected at the 5% significance level, the tiles in **c** are stippled. SM and VWC conditions with fewer than 20 samples are not shown. **d**, A map of the median

difference between post- and pre-fire $\frac{\Delta VWC}{\Delta t}$ binned into a 5° grid, SM and VWC conditions with fewer than ten samples are excluded. Areas with all conditions below this threshold are indicated by crosses. **e**, $\frac{\Delta VWC}{\Delta t}$ change relative to ΔNBR fire severity. The boxplots display median and 25th and 75th percentile of the distribution. The whiskers include approximately 99.3% of all datapoints, and outliers are not displayed.

loss (Fig. 1c). Post-fire acceleration of SM loss persists up to 3 months after fire (Extended Data Fig. 1). Fire impacts on $\frac{\Delta SM}{\Delta t}$ are present across the globe, with 67% of all areas we assess (aggregated into 5° spatial bins) experiencing a negative $\frac{\Delta SM}{\Delta t}$ change, thus showing accelerated SM loss (Fig. 1d). Several well-known large wildfire events, such as the 2019–2020 Southeast Australian fires^{33,34} or the 2017 Starbuck, 2016 Anderson Creek and 2017 Perryton grassland fires across the Oklahoma–Kansas–Texas border³⁵, are reflected in Fig. 1d. We use coarser-resolution SM from the European Space Agency Climate Change Initiative (ESA CCI)^{36–38} as a second SM dataset to confirm our findings. Observed fire effects on ESA CCI SM are much weaker; we only find a median increase of SM loss by 8% (Supplementary Fig. 1), which is also not very widespread with an increasing rate of SM loss for 55% of the analysed area. Although the acceleration of SM loss is apparent globally, the magnitude of the fire effect varies. Analysing SM loss relative to International Geosphere Biosphere Programme (IGBP) landcover classes³⁹, we find the largest acceleration in SM loss in broad-leaf forests (Extended Data Fig. 2). More severe fires, estimated by using ΔNBR, lead to a more negative $\frac{\Delta SM}{\Delta t}$ change, suggesting a positive relationship between fire severity and acceleration of SM loss (Fig. 1e).

Fast vegetation water uptake and growth post-fire

We used SMAP-based VWC to isolate the plant water dynamics following precipitation pulses. During drydowns, changes in VWC ($\frac{\Delta VWC}{\Delta t}$) can be both positive, indicating plant water uptake and growth, or negative, indicating plant wilting or mortality, with the regimes separated by a critical SM threshold⁷⁸ (Fig. 2a,b). When SM is above this threshold, $\frac{\Delta VWC}{\Delta t}$ is positive and tends to further increase with SM. Fire tends to increase the rate of positive VWC change, especially in areas with high SM and

VWC (Fig. 2c). A positive $\frac{\Delta VWC}{\Delta t}$ change is visible close to or even below the pre-fire critical SM threshold, suggesting that, post-fire, the vegetation maintains growth and water uptake at lower SM. Globally, we find a median $\frac{\Delta VWC}{\Delta t}$ change of 62%, this effect is extensive, with 67% of all 5° spatial bins experiencing positive $\frac{\Delta VWC}{\Delta t}$ changes (Fig. 2d). To evaluate the robustness of our findings on VWC, we also used VWC derived from the AMSR2 C-band VOD (Methods), which uses a different microwave frequency and retrieval algorithm than SMAP and can be more sensitive to herbaceous biomass and leaves. This additional analysis confirms our SMAP-based results, finding a median $\frac{\Delta VWC}{\Delta t}$ increase of 43%. Moreover, a positive $\frac{\Delta VWC}{\Delta t}$ response is prevalent in 70% of all 5° spatial bins (Supplementary Fig. 2). This further confirms widespread fast post-fire regeneration and changes in the sensitivity of $\frac{\Delta VWC}{\Delta t}$ to SM.

Faster post-fire vegetation water uptake is likely explained by the degree of vegetation regeneration relative to pre-fire conditions. We found that $\frac{\Delta VWC}{\Delta t}$ is higher after more severe fires, where vegetation regrowth can be fast. Rapid regeneration even after severe fires is expected given plant physiological adaptations to quickly regrow³³ and the high resource availability following fire⁴⁰. Furthermore, ecosystems responded differently, such that broadleaf forests experienced larger changes (Extended Data Fig. 3). Finally, fire effects on $\frac{\Delta VWC}{\Delta t}$ are more persistent than effects on $\frac{\Delta SM}{\Delta t}$, and lead to slightly faster VWC gains even in the subsequent growing season (Extended Data Fig. 4).

Fire effects shift diurnal plant–soil water relations

Given the large effects of fire on $\frac{\Delta VWC}{\Delta t}$ and $\frac{\Delta SM}{\Delta t}$, we hypothesize that components of these changes arise from altered plant hydraulic

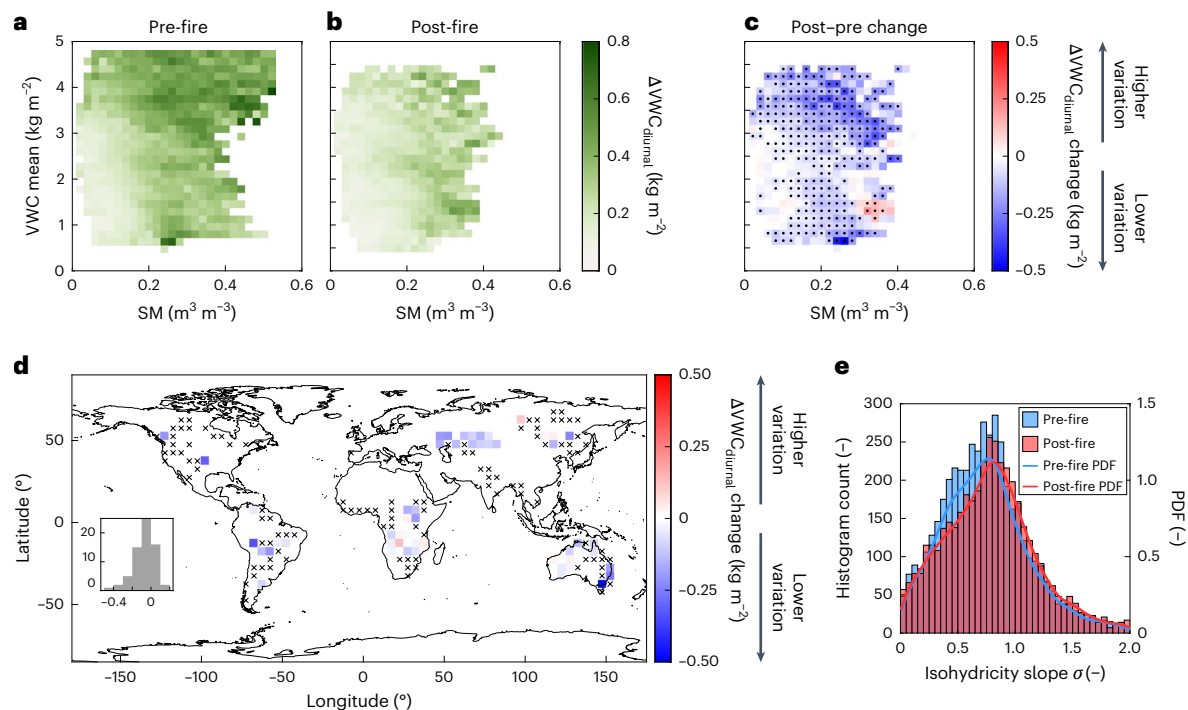


Fig. 3 | Fire changes diurnal VWC dynamics and isohyricity. **a–c**, Median pre-fire $\Delta VWC_{diurnal}$ (**a**), median post-fire $\Delta VWC_{diurnal}$ (**b**) and $\Delta VWC_{diurnal}$ post-minus pre-fire difference (**c**). We use a two-sided Wilcoxon rank sum test to determine if pre- and post-fire samples come from continuous distributions of equal mean. If this is rejected at the 5% significance level, the tiles in **c** are stippled. SM and VWC conditions with fewer than 20 samples are not displayed. **d**, A map of the mean difference between post- and pre-fire $\Delta VWC_{diurnal}$ binned into a 5° grid,

SM and VWC conditions with fewer than ten samples are excluded. Areas with all conditions below this threshold are indicated by crosses. **e**, Histograms of pre- and post-fire isohyricity slopes σ and kernel estimated probability density functions (PDFs). Based on a two-sided Wilcoxon rank sum test, we reject the hypothesis that pre- and post-fire samples come from distributions with equal means ($P = 1.6612 \times 10^{-8}$).

strategies. To test this, we analysed diurnal VWC changes because on such short timescales VWC can be informative regarding the level of plant stomatal control^{3,24,41,42} and the growth contribution to VWC changes is negligible. We used microwave-based VWC from AMSR2 in early morning (01:30) and midday (13:30) and calculated two metrics: (1) the absolute difference in VWC between early morning and midday ($\Delta VWC_{diurnal}$) and (2) the slope of the linear regression between early morning and midday VWCs (σ), which is a metric of isohyricity^{24,43}. The sensitivity of stomatal regulation to environmental factors can be simplified into the isohyricity framework, classifying a plant as isohyric if it exerts strong control on its daily VWC dynamics or as anisohyric if it exerts little to no control on its daily VWC dynamics^{24,43}. We find that fire reduced $\Delta VWC_{diurnal}$ across nearly all SM and VWC conditions (Fig. 3c), with a median $\Delta VWC_{diurnal}$ decrease of 30%. Globally, we observe a reduction in $\Delta VWC_{diurnal}$ across 73% of all 5° spatial bins. Furthermore, plants after fires tended to be more anisohyric (Fig. 3e). Our findings are consistent with observations at the field scale, where regenerating shrubs and grasses can display more anisohyric behaviour and might even sustain higher transpiration rates than pre-fire vegetation^{15,16}. This is supported by the fact that we find the strongest shift towards more anisohyric behaviour in forests and in areas that were more isohyric before the fire (Supplementary Figs. 3 and 4). In addition, shifts towards more anisohyric conditions are positively linked to fire severity (Supplementary Fig. 5). Taken together, these results provide evidence that fire changes the ecosystem water balance, by altering plant water relations on diurnal scales.

Fire effects on SM pulse usage across ecosystems

Our results suggest that fire disturbance changes the way SM pulses are used, leading to faster SM loss, faster VWC gain and an increased coupling between SM losses and VWC gains and, thus, a higher

sensitivity of VWC to SM pulses post-fire (Extended Data Fig. 5). We confirm the increased coupling using linear models, which demonstrate a stronger relationship between post-fire $\frac{\Delta SM}{\Delta t}$ and $\frac{\Delta VWC}{\Delta t}$ (Extended Data Table 1).

We find evidence that this is related to more anisohyric ecosystem behaviour post-fire, with landcover classes with stronger shifts towards anisohyricity (that is, evergreen broadleaf forest) experiencing faster SM losses (Supplementary Fig. 3). This shift in isohyricity is also linked to fire severity (Supplementary Fig. 5), as relative regeneration and shifts in plant community composition might be larger following severe fires^{40,44}. This expands on previous studies on SM and VWC coupling^{7,45} and gives evidence that the VWC response to SM pulses can be strongly conditioned by fire events.

Our findings are especially applicable to drylands, where SM pulses are followed by a cascade of biological activity, resulting in plant growth and gains in VWC (that is, the pulse-reserve paradigm)⁷⁴⁶. Because fires are common in many dryland systems, they may play an important role in modifying these pulse-reserve processes.

Several other processes probably contribute to our findings, although it is not possible to quantify their magnitude on observed SM and VWC directly on our study scale. For example, smoke can affect cloud formation⁴⁷ as well as precipitation^{48,49}, which could alter incoming shortwave radiation. Furthermore, hydraulic properties can change through a buildup of hydrophobicity or combustion products such as ash⁵⁰. Soil water repellency and ash accumulation can alter the soil water retention curve, potentially lowering the tension holding water in the soil matrix, which could support faster relative SM loss through evapotranspiration or drainage. It is not possible to quantify changes in water retention directly from remote sensing techniques, but we find that the relationship between $\frac{\Delta SM}{\Delta t}$ and SM in our linear models does not vary between pre- and post-fire state (Extended Data Table 1). This

suggests that water retention is either not altered substantially by fire or does not affect SM losses in our study.

Limited evidence of climatic variables as confounders

To further account for climatic differences in pre- and post-fire conditions that may influence $\frac{\Delta SM}{\Delta t}$, $\frac{\Delta VWC}{\Delta t}$ and $\Delta VWC_{diurnal}$, we test whether faster SM loss after a fire could be driven by higher VPD. We analyse VPD from the Atmospheric Infrared Sounder (AIRS) and from the fifth generation of the European Reanalysis (ERA5-Land) and find no evidence of consistent differences between pre- and post-fire VPD (Extended Data Fig. 6 and Supplementary Fig. 6). VPD increased across some SM and VWC conditions, but when analysed for 5° spatial bins, only 50% and 48% of the bins exhibited increasing VPD. However, higher VPD after fire, which could also explain faster SM loss, tended to be more prevalent in severely burned areas. Effects of fire on VPD might dampen much faster than effects on SM and VWC as processes like advection and synoptic scale atmospheric dynamics can change on the timescale of days and could mask signals caused by fire. Plant–soil water relations are changed not only by fire but also by seasonal growing dynamics and other disturbances such as droughts.

To quantify the impact of these events relative to the observed fire effects, we compare burned pixels with nearby unburned pixels under similar climatic conditions. Instead of analysing $\frac{\Delta SM}{\Delta t}$, $\frac{\Delta VWC}{\Delta t}$ and $\Delta VWC_{diurnal}$ relative to a fire event, we analyse them relative to the timing of the lowest VWC value in our study period, which corresponds to the maximum impact of a non-fire disturbance. In contrast to fire, there were no consistent directional effects, that is, we did not find accelerated SM loss, faster gains in VWC or more anisohydric conditions (Extended Data Figs. 7–9). Thus, fire as a disturbance has a unique impact on plant–soil water relations.

Overall, we find strong global evidence for wildfires accelerating SM loss and leading to more vigorous post-fire VWC gain. Both effects are consistent across ecosystems, although largest in forests, and are exacerbated by fire severity. Surprisingly, SM loss and VWC gain were relatively unrelated to VPD, pointing to ecosystem level systematic changes in plant–soil water relations, namely a stronger coupling between VWC gain and SM loss as a controlling mechanism. This finding is further supported by shifts towards higher anisohydricity in post-fire vegetation, which is most prominent in forests and previously isohydric areas and positively related to fire severity. Consequently, fire intensifies the coupling between plant and soil water cycling, which will likely strengthen as wildfires become more severe and common.

Online content

Any methods, additional references, Nature Portfolio reporting summaries, source data, extended data, supplementary information, acknowledgements, peer review information; details of author contributions and competing interests; and statements of data and code availability are available at <https://doi.org/10.1038/s41561-024-01563-6>.

References

1. D'Odorico, P., Caylor, K., Okin, G. S. & Scanlon, T. M. On soil moisture-vegetation feedbacks and their possible effects on the dynamics of dryland ecosystems. *J. Geophys. Res. Biogeosci.* **112**, G04010 (2007).
2. Tian, F. et al. Coupling of ecosystem-scale plant water storage and leaf phenology observed by satellite. *Nat. Ecol. Evol.* **2**, 1428–1435 (2018).
3. Konings, A. G., Williams, A. P. & Gentine, P. Sensitivity of grassland productivity to aridity controlled by stomatal and xylem regulation. *Nat. Geosci.* **10**, 284–288 (2017).
4. Fu, Z. et al. Atmospheric dryness reduces photosynthesis along a large range of soil water deficits. *Nat. Commun.* **13**, 989 (2022).
5. Schlesinger, W. H. & Jasechko, S. Transpiration in the global water cycle. *Agric. For. Meteorol.* **189–190**, 115–117 (2014).
6. Jasechko, S. et al. Terrestrial water fluxes dominated by transpiration. *Nature* **496**, 347–350 (2013).
7. Feldman, A. F. et al. Moisture pulse-reserve in the soil–plant continuum observed across biomes. *Nat. Plants* **4**, 1026–1033 (2018).
8. Fu, Z. et al. Critical soil moisture thresholds of plant water stress in terrestrial ecosystems. *Sci. Adv.* **8**, 1–13 (2022).
9. Roces-Díaz, J. V., Santín, C., Martínez-Vilalta, J. & Doerr, S. H. A global synthesis of fire effects on ecosystem services of forests and woodlands. *Front. Ecol. Environ.* **20**, 170–178 (2022).
10. Seidl, R. et al. Forest disturbances under climate change. *Nat. Publ. Gr.* **7**, 395–402 (2017).
11. Anderegg, W. R. L. et al. A climate risk analysis of Earth's forests in the 21st century. *Science* **377**, 1099–1103 (2022).
12. Alizadeh, M. R. et al. Warming enabled upslope advance in western US forest fires. *Proc. Natl Acad. Sci. USA* **118**, e2009717118 (2021).
13. Boer, M. M., De Dios, V. R., Stefaniak, E. Z. & Bradstock, R. A. A hydroclimatic model for the distribution of fire on Earth. *Environ. Res. Commun.* **3**, 035001 (2021).
14. O, S., Hou, X. & Orth, R. Observational evidence of wildfire-promoting soil moisture anomalies. *Sci. Rep.* **10**, 11008 (2020).
15. Cooper, C. E. et al. Transpiration in recovering mixed loblolly pine and oak stands following wildfire in the Lost Pines region of Texas. *Ecophysiology* **12**, e2052 (2019).
16. Poulos, H. M., Barton, A. M., Koch, G. W., Kolb, T. E. & Thode, A. E. Wildfire severity and vegetation recovery drive post-fire evapotranspiration in a southwestern pine-oak forest, Arizona, USA. *Remote Sens. Ecol. Conserv.* **7**, 579–591 (2021).
17. Shakesby, R. & Doerr, S. Wildfire as a hydrological and geomorphological agent. *Earth Sci. Rev.* **74**, 269–307 (2006).
18. Wine, M. L. & Cadol, D. Hydrologic effects of large southwestern USA wildfires significantly increase regional water supply: fact or fiction? *Environ. Res. Lett.* **11**, 085006 (2016).
19. Collar, N. M. et al. Linking fire-induced evapotranspiration shifts to streamflow magnitude and timing in the western United States. *J. Hydrol.* **612**, 128242 (2022).
20. Seidl, R. & Turner, M. G. Post-disturbance reorganization of forest ecosystems in a changing world. *Proc. Natl Acad. Sci. USA* **119**, 1–10 (2022).
21. Akbar, R. et al. Estimation of landscape soil water losses from satellite observations of soil moisture. *J. Hydrometeorol.* **19**, 871–889 (2018).
22. Jones, M. O., Kimball, J. S. & Jones, L. A. Satellite microwave detection of boreal forest recovery from the extreme 2004 wildfires in Alaska and Canada. *Glob. Chang. Biol.* **19**, 3111–3122 (2013).
23. Bousquet, E., Mialon, A., Rodriguez-Fernandez, N., Mermoz, S. & Kerr, Y. Monitoring post-fire recovery of various vegetation biomes using multi-wavelength satellite remote sensing. *Biogeosciences* **19**, 3317–3336 (2022).
24. Konings, A. G. & Gentine, P. Global variations in ecosystem-scale isohydricity. *Glob. Chang. Biol.* **23**, 891–905 (2017).
25. Alonso-González, E. & Fernández-García, V. MOSEV: a global burn severity database from MODIS (2000–2020). *Earth Syst. Sci. Data* **13**, 1925–1938 (2021).
26. Saberi, S. J. & Harvey, B. J. What is the color when black is burned? Quantifying (re)burn severity using field and satellite remote sensing indices. *Fire Ecol.* **19**, 24 (2023).
27. Miller, J. D. & Thode, A. E. Quantifying burn severity in a heterogeneous landscape with a relative version of the delta Normalized Burn Ratio (dNBR). *Remote Sens. Environ.* **109**, 66–80 (2007).

28. Shellito, P. J. et al. SMAP soil moisture drying more rapid than observed in situ following rainfall events. *Geophys. Res. Lett.* **43**, 8068–8075 (2016).
29. Or, D., Lehmann, P., Shahraeeni, E. & Shokri, N. Advances in soil evaporation physics—a review. *Vadose Zo. J.* **12**, vzi2012.0163 (2013).
30. McColl, K. A. et al. Global characterization of surface soil moisture drydowns. *Geophys. Res. Lett.* **44**, 3682–3690 (2017).
31. Pan, F. & Peters-Lidard, C. D. On the relationship between mean and variance of soil moisture fields. *J. Am. Water Resour. Assoc.* **44**, 235–242 (2008).
32. Carminati, A. et al. Dynamics of soil water content in the rhizosphere. *Plant Soil* **332**, 163–176 (2010).
33. Qin, Y. et al. Large loss and rapid recovery of vegetation cover and aboveground biomass over forest areas in Australia during 2019–2020. *Remote Sens. Environ.* **278**, 113087 (2022).
34. Godfree, R. C. et al. Implications of the 2019–2020 megafires for the biogeography and conservation of Australian vegetation. *Nat. Commun.* **12**, 1023 (2021).
35. Steiner, J. L. et al. Grassland wildfires in the Southern Great Plains: monitoring ecological impacts and recovery. *Remote Sens.* **12**, 619 (2020).
36. Dorigo, W. A. et al. ESA Soil Moisture Climate Change Initiative (Soil_Moisture_cci): COMBINED product, Version 06.1. NERC EDS Centre for Environmental Data Analysis <https://catalogue.ceda.ac.uk/uuid/43d73291472444e6b9c2d2420dbad7d6> (2021).
37. Gruber, A., Scanlon, T., van der Schalie, R., Wagner, W. & Dorigo, W. Evolution of the ESA CCI Soil Moisture climate data records and their underlying merging methodology. *Earth Syst. Sci. Data* **11**, 717–739 (2019).
38. Preimesberger, W., Scanlon, T., Su, C.-H., Gruber, A. & Dorigo, W. Homogenization of structural breaks in the Global ESA CCI Soil Moisture Multisatellite Climate Data Record. *IEEE Trans. Geosci. Remote Sens.* **59**, 2845–2862 (2021).
39. Belward, A. S., Estes, J. E., Kline, K. D., Estes, T. E. & Kline, K. D. The IGBP-DIS Global 1-Km Land-Gover Data Set DlsGover: a project overview. *Photogramm. Eng. Remote Sens.* **65**, 1013–1020 (1999).
40. Pausas, J. G. & Keeley, J. E. Evolutionary ecology of resprouting and seeding in fire-prone ecosystems. *New Phytol.* **204**, 55–65 (2014).
41. Knipfer, T. et al. Predicting stomatal closure and turgor loss in woody plants using predawn and midday water potential. *Plant Physiol.* **184**, 881–894 (2020).
42. Carminati, A. & Javaux, M. Soil rather than xylem vulnerability controls stomatal response to drought. *Trends Plant Sci.* **25**, 868–880 (2020).
43. Martínez-Vilalta, J., Poyatos, R., Aguadé, D., Retana, J. & Mencuccini, M. A new look at water transport regulation in plants. *New Phytol.* **204**, 105–115 (2014).
44. Thomsen, A. M. & Ooi, M. K. J. Shifting season of fire and its interaction with fire severity: impacts on reproductive effort in resprouting plants. *Ecol. Evol.* **12**, 1–12 (2022).
45. Feldman, A. F., Chulakadabba, A., Short Gianotti, D. J. & Entekhabi, D. Landscape-scale plant water content and carbon flux behavior following moisture pulses: from dryland to mesic environments. *Water Resour. Res.* **57**, 1–20 (2021).
46. Noy-Meir, I. Desert ecosystems: environment and producers. *Annu. Rev. Ecol. Syst.* **4**, 25–51 (1973).
47. Herbert, R., Stier, P. & Dagan, G. Isolating large-scale smoke impacts on cloud and precipitation processes over the Amazon with convection permitting resolution. *J. Geophys. Res. Atmos.* **126**, e2021JD034615 (2021).
48. Li, F., Lawrence, D. M., Jiang, Y., Liu, X. & Lin, Z. Fire aerosols slow down the global water cycle. *J. Clim.* **35**, 7219–7233 (2022).
49. Rosenfeld, D. TRMM observed first direct evidence of smoke from forest fires inhibiting rainfall. *Geophys. Res. Lett.* **26**, 3105–3108 (1999).
50. Stoof, C. R., Wesseling, J. G. & Ritsema, C. J. Effects of fire and ash on soil water retention. *Geoderma* **159**, 276–285 (2010).

Publisher's note Springer Nature remains neutral with regard to jurisdictional claims in published maps and institutional affiliations.

Open Access This article is licensed under a Creative Commons Attribution 4.0 International License, which permits use, sharing, adaptation, distribution and reproduction in any medium or format, as long as you give appropriate credit to the original author(s) and the source, provide a link to the Creative Commons licence, and indicate if changes were made. The images or other third party material in this article are included in the article's Creative Commons licence, unless indicated otherwise in a credit line to the material. If material is not included in the article's Creative Commons licence and your intended use is not permitted by statutory regulation or exceeds the permitted use, you will need to obtain permission directly from the copyright holder. To view a copy of this licence, visit <http://creativecommons.org/licenses/by/4.0/>.

© The Author(s) 2024

Methods

Datasets

In this study we use nearly 6 years (1 April 2015 to 31 December 2020) of SM and VOD from the SMAP mission and VOD from the AMSR2 system onboard the GCOM-1 satellite. Both SMAP and AMSR2 have revisit times of at least 3 days over most of the globe, which is high enough to sufficiently resolve short-term plant–soil water relations^{51–53}. SM and VOD from SMAP L-band observations are retrieved using the Multi-Temporal Dual Channel Algorithm (MT-DCA), version 4^{54,55}, which has been applied in multiple studies analysing plant–soil water dynamics^{7,56}. The approach uses two consecutive satellite overpasses, which leads to more reliable SM and VOD retrievals⁵⁷. SMAP observations have a sensing depth of approximately 10 cm (ref. 58), which is modulated by the soil conditions and the vegetation layer attenuating the soil emission. With increasing vegetation, the penetration through the canopy decreases, which makes the estimation of SM and VOD more uncertain⁵⁹. In this study, we nearly exclusively analyse drydowns with a VOD lower than 1, or a VWC equivalent of less than 9 kg m⁻², which is much lower than the highest VOD values of approximately 1.4 retrieved by the MT-DCA. This means that retrieval errors due to strong vegetation effects should be relatively limited at L-band. Even if SM and VOD are retrieved with lower accuracy in strongly vegetated areas, this should affect only a small range of the analysed SM–VWC conditions, and fire effects are visible across low and high VWC conditions. The emission depth of the microwave signal from the soil can change depending on SM present, soil properties and litter cover^{60,61}. Some of these aspects might be changed by fire and could potentially affect SM loss. Previous studies suggested that SMAP drydowns are faster than station data because they are representative of a shallower profile²⁸, which dries out more quickly²⁹, so only a systematic shift to shallower emission depths could explain accelerated SM losses after fire. This seems unlikely across the wide biomes we cover, some of which have very little litter. Moreover, emission depth constantly changes depending on SM saturation in the soil, something we account for by only comparing the same SM conditions. Other sources of uncertainty in SM and VOD retrievals normally lead to positively correlated errors in SM and VOD, which is the opposite of the directionality we observe in post-fire drydowns (SM decreases and VOD increases). The MT-DCA dataset is gridded at 9 km pixel resolution using the Equal-Area Scalable Earth 2 (EASE2) grid⁶². We use the ESA CCI COMBINED SM product, version 06.1^{36,37,63} as a second independent dataset to assess changes in SM dynamics. It comes at a resolution of 0.25°; thus, it is substantially coarser than SMAP SM and VOD. For our binning process, we need a VOD dataset of same spatial resolution; therefore, we include the Global Long-term Microwave Vegetation Optical Depth Climate Archive VODCA VOD⁶⁴. We use the version 01.0.0 X-band VOD product. To assess isohydricity and diurnal VWC changes, we use the C-band AMSR2 VOD from the Land Parameter Retrieval Model L3 product, version V001^{65,66}, at an original resolution of 10 km. We regrid the C-band VOD to 9 km EASE2-grid. We use both descending, 1:30, and ascending, 13:30, overpasses to assess diurnal changes in VWC⁶⁷. The VOD at L- and C-bands is substantially different; the C-band generally follows leaf phenology and optical remote sensing indices such as Normalized Difference Vegetation Index and leaf area index, whereas the L-band VOD is phase shifted relative to the C-band VOD and optical indices^{68,69}. Studies suggest that the L-band is more indicative of the water content in larger vegetation constituents (for example, stems), while the C-band is most indicative of leaf water content^{2,69,70}.

VOD can be linearly related to VWC⁷¹. Here, we use constant factors of 0.11 (L-band) and 0.2046 (C- and X-band) across all ecosystems. This is equivalent to the L-band conversion applied by ref. 7. For the C-band, we rely on the average of all values reported by ref. 72 for multiple vegetation types. Overall, the conversion from VOD to VWC is a linear scaling and does not affect any of our results other than providing more intuitive axis dimensions and units.

We calculate daytime VPD using relative humidity and air temperature from the AIRS on the National Aeronautics and Space Administration's Aqua satellite⁷³. We use the AIRS version 7 Level 3 product⁷⁴. VPD is in units of kilopascal and has a 1° resolution. Although this is much coarser than the 9 km resolution of the SM and VWC datasets, we believe it sufficiently captures large-scale atmospheric dryness dynamics. As a result of the lower spatial resolution, figures depicting VPD will rely on a lower number of total samples. To further test the role of VPD and overcome the lower resolution of AIRS VPD, we include midday VPD from ERA5-Land hourly data as well⁷⁵. ERA5-Land VPD has a resolution of 0.1° and is regridded to the 9 km EASE2-grid.

For the identification of fire events and burn date, we use the MOSEV global burn severity database²⁵, which provides burn date as well as burn severity (ΔNBR) based on the Moderate-Resolution Imaging Spectroradiometer (MODIS) on both Aqua and Terra satellites. The database is organized using MODIS tiles and has a resolution of 500 m. The MOSEV database applies clouds and snow filtering and shows good agreement with Landsat products²⁵. Based on the temporal coverage of the MOSEV database and the microwave datasets, our study period is from 1 April 2015 to 31 December 2020. To assess fire effects relative to landcover classes, we use the IGBP landcover classification³⁹.

Fire detection at the 9 km pixel scale

We hypothesize that a large part of a SMAP 9 km pixel has to burn within a short time for fire to affect plant–soil water relations. Therefore, we consider a SMAP pixel for our analysis if at least 300 MOSEV pixels associated with a SMAP pixel have burned within 60 days. This leads to 11,027 SMAP pixels being considered burned during our study period, with 18% of them experiencing more than one fire event.

We associate SMAP and MOSEV pixels on the basis of their centre coordinates. The threshold of 300 burned MODIS pixels is very high, as there are approximately 324 MOSEV pixels in one SMAP pixel, which guarantees that all SMAP pixels we analyse have been burned to a large extent and within a short time. If MOSEV burn detections have reached the previously mentioned threshold, we use the earliest and latest MOSEV burn dates within the 60 days with at least 300 burned MODIS pixels to define the start and end of a fire event for the associated SMAP pixel. This definition of burn start and end dates is likely to underestimate maximum fire effects, as some MOSEV pixels have already burnt and started recovery by the time the burn end date is defined for the SMAP pixel. Identifying the end of a fire event can be challenging due to the potential presence of persistent small fires that might not be detected at MODIS 500 m resolution^{76,77}. Here, this is unlikely due to our focus on very large and fast burning fire events, which have only a small contribution of small-scale fires to total burned area. This and the fact that we analyse drydowns that follow after precipitation events make it unlikely that undetected small-scale fires are confounding our results. For each burned SMAP pixel, we calculate the temporal distance between each drydown and the closest fire event, using the minimum distance as a metric in our analysis. If a SMAP pixel is burned multiple times, we still use the minimum distance to the closest fire event to categorize a drydown as pre- or post-fire. We believe this is a conservative approach, especially as the effects of subsequent fires on $\frac{\Delta SM}{\Delta t}$ and $\frac{\Delta VPD}{\Delta t}$ should be weaker than the effects of the first fire. We think this will weaken the observed fire effects rather than enhancing them.

Drydown detection and characterization of plant–soil water relations

We define a drydown as a series of at least four consecutive observations of decreasing SM^{30,78} (equivalent to at least 4 days close to the poles and 12 days at the Equator). We only extract drydowns for 9 km SMAP pixels that burn during our study. SM, VOD and VPD are extracted for the duration of all detected drydowns. We compared the distribution of drydown length pre- and post-fire and find nearly no difference. SM conditions are very similar as well, although post-fire conditions

are slightly wetter (Supplementary Fig. 7). Checking the effects of drydown lengths on our $\frac{\Delta SM}{\Delta t}$ results we find very little difference between short (length 4) and longer (length ≥ 5) drydowns. Extracted SM, VWC and VPD are corrected for seasonal dynamics by subtracting a 120-day moving average from each time series. After extracting drydowns from the smoothed time series, their slope is used to correct the original drydowns. We evaluated the effects of correcting for seasonality using both a 365-day moving average and no smoothing at all. The overall effect of the smoothing correction on drydown slopes was minor and did not substantially affect any pre- to post-fire differences. We extracted a total of 661,605 drydowns, but not all of them are analysed as we only consider the ones closely following a fire and a pre-fire reference period. This amounts to a total of 19,191 pre-fire and 10,934 post-fire drydowns. We compute mean rates of change as finite differences over the sampled period via

$$\frac{\Delta SM}{\Delta t} = SM_{t+1} - SM_t \quad (1)$$

$$\frac{\Delta VWC}{\Delta t} = VWC_{t+1} - VWC_t \quad (2)$$

$$\frac{\Delta VPD}{\Delta t} = VPD_{t+1} - VPD_t \quad (3)$$

Afterwards and in line with ref. 7, rates of change are interpolated to a $0.01 \text{ m}^3 \text{ m}^{-3} \text{ SM}$ scale. The interpolation step does not change the slopes of the rates of change and is primarily done to enable efficient binning based on SM and VWC conditions.

Isolating fire effects on plant–soil water relations

Climatic conditions pre- and post-fire are distinct; not only are there systematic differences in SM and VWC, but there are also different stages of vegetation seasonality and plant activity. This makes it difficult to distinguish fire effects from the underlying seasonality affecting $\frac{\Delta SM}{\Delta t}$ and $\frac{\Delta VWC}{\Delta t}$. We want to avoid interpreting the effect seasonality has on these signals and isolate changes in $\frac{\Delta SM}{\Delta t}$ and $\frac{\Delta VWC}{\Delta t}$ related to fire effects only. To do this, we apply four steps:

1. We remove a seasonal component from SM, VWC and VPD using a 120-day moving average.
2. We characterize plant–soil water relations relative to the SM and VWC states. We find that $\frac{\Delta SM}{\Delta t}$ and $\frac{\Delta VWC}{\Delta t}$ strongly depend on the respective SM and VWC states. The dependence on SM follows from the theory of soil water retention curves³², and has been observed with SMAP SM observations²¹. The dependence on VWC follows from the impact of vegetation on evapotranspiration and other processes contributing to SM losses. Consequently, we bin analysed variables into a 30×30 grid of SM and VWC conditions and only keep bins with more than 20 samples per bin. For all maps and boxplots, we use 20×20 bins to increase the sample size per bin and only keep bins with at least ten samples per bin. If a spatial 5° -by- 5° bin does not have any SM and VWC conditions with more than ten samples, it is indicated by a cross in all our map figures. This removes systematic differences in pre- and post-fire SM and VWC states. If applicable, we only compare variables at the same SM and VWC states. Not doing this leads to only negligible differences in pre- to post-fire SM and VWC rates of change (Supplementary Fig. 8).
3. Instead of comparing SM, VWC and VPD directly before and after a fire event, we compare post-fire conditions with the same time in the previous years. We compare 0–30 days post-fire with the same 30 days in up to 4 years (if available) pre-fire, therefore only comparing the same season. This is done con-

sistently for pre- and post-fire periods in all our analyses. We use all drydowns from up to 4 years pre-fire, thus representing the average pre-fire conditions from all available data.

4. We randomly select unburned 9 km pixels as a reference for our analysis. We select pixels within a certain spatial proximity to burned pixels but check that they do not have any burns detected at the 500 m MODIS scale. We select the same number of unburned reference pixels as burned pixels for each MODIS tile. We end up with 11,027 unburned reference pixels, and their spatial distribution is similar to that of the burned pixels. This guarantees similarity in climatic conditions and vegetation seasonality. As there are no detected burns, we find the date of the lowest VOD for each reference pixel, after smoothing the VOD time series using a 120-day moving average. This is equivalent to the lowest VWC state caused by seasonality and other disturbances. Comparing 30 days after the lowest VWC state with the same time in the previous year should give an indication of how strongly plant–soil water relations vary due to droughts or other non-fire disturbances. We repeat all processing steps and analyses for the reference pixels and show the results in Extended Data Figs. 7–9.

Fire severity

We estimate fire severity using changes in NBR from pre- to post-fire. This difference, called ΔNBR is reported in the MOSEV database for every 500 m MODIS pixel. For every burned 9 km SMAP pixel, we average reported ΔNBR values into one 9 km value. NBR and ΔNBR are among the most used spectral indices for the assessment of fire effects⁷⁹. NBR is similar to the Normalized Difference Vegetation Index in respect to the used spectral bands⁸⁰; a higher value relates to a higher contribution of vegetation to the signal. Previous studies have found a comparable performance of VOD and NBR in describing fire severity⁸¹, although NBR and ΔNBR can be affected by clouds and other atmospheric effects. Overall, ΔNBR is considered one of the most standard remote sensing metrics to assess fire severity.

Estimation of $\Delta VWC_{\text{diurnal}}$ and isohydricity σ from C-band VOD

On diurnal timescales, we can assume any growth contribution on VWC to be negligible; thus, diurnal changes in VWC fully isolate plant water dynamics. Diurnal VWC dynamics are of special interest because they are closely related to the level of stomatal control plants apply^{3,24,41,42}. The sensitivity of stomatal conductance to environmental factors can be simplified into the so-called isohydricity framework, classifying a plant as isohydric if it exerts strong control on its daily VWC dynamics or as anisohydric if it exerts little to no control on its daily VWC dynamics^{24,43}. Consequently, measurements of pre-dawn and midday leaf water potential have been used to assess the level of plant isohydricity and predict stomatal closure^{41,82}. Microwave-based VWC can be used to derive ecosystem-scale isohydricity estimates, which can serve as predictors of grassland productivity³ or wildfire vulnerability⁸³. Here, we use AMSR2 C-band VWC to calculate the diurnal range of VWC, $\Delta VWC_{\text{diurnal}}$ and the isohydricity slope σ . σ is zero for a fully isohydric plant and 1 or higher for a perfectly anisohydric plant. To calculate isohydricity, we follow the methodology described in ref. 24 (Methods).

We use AMSR2 C-band VOD from ascending (13:30) and descending (1:30) overpasses during the 30-day pre- and post-fire periods to estimate σ . Following refs. 24,84, we use the linear slope of the regression between midday and midnight VOD as an indicator of isohydricity

$$VOD^{\text{midday}} = \sigma VOD^{\text{midnight}} + \Lambda. \quad (4)$$

Λ denotes the intercept of the regression. In line with ref. 24, we remove observations with $VOD^{\text{midday}} > VOD^{\text{midnight}}$ as these observations might be related to incomplete overnight refilling. References^{24,84} used X-band

(10.7 GHz) observations for their isohydricity estimation, but C- and X-bands from the same sensor are extremely similar in seasonality and short-term dynamics^{69,70,85}. σ is unaffected by a scaling to VWC; therefore, it is directly estimated from VOD. Furthermore, we calculate $\Delta\text{VWC}_{\text{diurnal}}$, which is the difference between $\text{VWC}_{\text{midnight}}$ and $\text{VWC}_{\text{midday}}$. While σ is a metric of the co-regulation of day and night water content, $\Delta\text{VWC}_{\text{diurnal}}$ assesses the magnitude of diurnal VWC dynamics.

Data availability

All datasets used in this study are publicly available. SMAP SM and VOD are available from Zenodo at <https://zenodo.org/record/5579549#.YZvbPS1h1QI> (ref. 55). The MOSEV fire severity database is available from Zenodo at <https://zenodo.org/record/4265209> (ref. 86). AMSR2 ascending and descending VOD is available from https://disc.gsfc.nasa.gov/datasets/LPRM_AMSR2_DS_D_SOILM3_001/summary. AIRS VPD is available from https://disc.gsfc.nasa.gov/datasets/AIRS3STD_7.0/summary. ESA CCI SM is available from <https://doi.org/10.5285/2893555223242ca97953a8db99c2821>. VPD from ERA is available from <https://doi.org/10.24381/cds.e2161bac>.

Code availability

All codes essential for this analysis are available via Zenodo at <https://doi.org/10.5281/zenodo.13768695> (ref. 87).

References

- Entekhabi, D. et al. The soil moisture active passive (SMAP) mission. *Proc. IEEE* **98**, 704–716 (2010).
- Imaoka, K. et al. Instrument performance and calibration of AMSR-E and AMSR2. *ISPRS Arch.* **XXXVIII**, 13–16 (2010).
- Imaoka, K. et al. Global Change Observation Mission (GCOM) for monitoring carbon, water cycles, and climate change. *Proc. IEEE* **98**, 717–734 (2010).
- Konings, A. G., Piles, M., Das, N. & Entekhabi, D. L-band vegetation optical depth and effective scattering albedo estimation from SMAP. *Remote Sens. Environ.* **198**, 460–470 (2017).
- Feldman, A. F., Konings, A. G., Piles, M. & Entekhabi, D. The Multi-Temporal Dual Channel Algorithm (MT-DCA) (Version 4). Zenodo <https://doi.org/10.5281/zenodo.5579549> (2021).
- Feldman, A. F., Short Gianotti, D. J., Konings, A. G., Gentile, P. & Entekhabi, D. Patterns of plant rehydration and growth following pulses of soil moisture availability. *Biogeosciences* <https://doi.org/10.5194/bg-2020-380> (2020).
- Feldman, A. F., Chaparro, D. & Entekhabi, D. Error propagation in microwave soil moisture and vegetation optical depth retrievals. *IEEE J. Sel. Top. Appl. Earth Obs. Remote Sens.* **14**, 11311–11323 (2021).
- Feldman, A. F. et al. Remotely Sensed Soil Moisture Can Capture Dynamics Relevant to Plant Water Uptake. *Water Resour. Res.* **59**, e2022WR033814 (2023).
- Baur, M. J. et al. Time-variations of zeroth-order vegetation absorption and scattering at L-band. *Remote Sens. Environ.* **267**, 112726 (2021).
- Kurum, M. et al. Impact of conifer forest litter on microwave emission at L-band. *IEEE Trans. Geosci. Remote Sens.* **50**, 1071–1084 (2012).
- Feldman, A. F. et al. Satellites capture soil moisture dynamics deeper than a few centimeters and are relevant to plant water uptake. *Earth Sp. Sci. Open Arch.* <https://doi.org/10.1002/essoar.10511280.1> (2022).
- Brodzik, M. J., Billingsley, B., Haran, T., Raup, B. & Savoie, M. H. EASE-Grid 2.0: incremental but significant improvements for Earth-gridded data sets. *ISPRS Int. J. Geo-Inf.* **1**, 32–45 (2012).
- Dorigo, W. et al. ESA CCI soil moisture for improved Earth system understanding: state-of-the art and future directions. *Remote Sens. Environ.* **203**, 185–215 (2017).
- Moesinger, L. et al. The global long-term microwave Vegetation Optical Depth Climate Archive (VODCA). *Earth Syst. Sci. Data* **12**, 177–196 (2020).
- Owe, M., de Jeu, R. & Holmes, T. Multisensor historical climatology of satellite-derived global land surface moisture. *J. Geophys. Res.* **113**, F01002 (2008).
- Vrije Universiteit Amsterdam (de Jeu, R.) & NASA GSFC (Owe, M.). AMSR2/GCOM-W1 surface soil moisture (LPRM) L3 1 day 10 km x 10 km ascending V001. *Goddard Earth Sciences Data and Information Services Center (GES DISC)* <https://doi.org/10.5067/BOGHODHJLDA8> (2014).
- Vrije Universiteit Amsterdam (de Jeu, R.) & NASA GSFC (Owe, M.). AMSR2/GCOM-W1 surface soil moisture (LPRM) L3 1 day 10 km x 10 km descending V001. *Goddard Earth Sciences Data and Information Services Center (GES DISC)* <https://doi.org/10.5067/M5DTR2QUYLS2> (2014).
- Li, X. et al. Compared performances of SMOS-IC soil moisture and vegetation optical depth retrievals based on tau-omega and two-stream microwave emission models. *Remote Sens. Environ.* **236**, 111502 (2020).
- Baur, M. J., Jagdhuber, T., Feldman, A. F., Akbar, R. & Entekhabi, D. Estimation of relative canopy absorption and scattering at L-, C- and X-bands. *Remote Sens. Environ.* **233**, 111384 (2019).
- Teubner, I. E. et al. Assessing the relationship between microwave vegetation optical depth and gross primary production. *Int. J. Appl. Earth Obs. Geoinf.* **65**, 79–91 (2018).
- Jackson, T. J. & Schmugge, T. J. Vegetation effects on the microwave emission of soils. *Remote Sens. Environ.* **36**, 203–212 (1991).
- Van de Griend, A. A. & Wigneron, J.-P. The b-factor as a function of frequency and canopy type at H-polarization. *IEEE Trans. Geosci. Remote Sens.* **42**, 786–794 (2004).
- Aumann, H. H. & Pagano, R. J. Atmospheric infrared sounder on the earth observing system. *Opt. Eng.* **33**, 776–784 (1994).
- AIRS project. Aqua/AIRS L3 Daily Standard Physical Retrieval (AIRS-only) 1 degree x 1 degree V7.0. *Goddard Earth Sciences Data and Information Services Center (GES DISC)* <https://doi.org/10.5067/UO3Q64CTTS1U> (2019).
- Muñoz Sabater, J. ERA5-Land hourly data from 1950 to present. *Copernicus Climate Change Service Climate Data Store* <https://doi.org/10.24381/cds.e2161bac> (2019).
- Ramo, R. et al. African burned area and fire carbon emissions are strongly impacted by small fires undetected by coarse resolution satellite data. *Proc. Natl Acad. Sci. USA* **118**, 1–7 (2021).
- Andela, N. et al. The Global Fire Atlas of individual fire size, duration, speed and direction. *Earth Syst. Sci. Data* **11**, 529–552 (2019).
- Sehgal, V., Gaur, N. & Mohanty, B. P. Global surface soil moisture drydown patterns. *Water Resour. Res.* **57**, 1–26 (2021).
- Kurbanov, E. et al. Remote sensing of forest burnt area, burn severity, and post-fire recovery: a review. *Remote Sens.* **14**, 4714 (2022).
- Alcaras, E., Costantino, D., Guastaferro, F., Parente, C. & Pepe, M. Normalized Burn Ratio Plus (NBR+): a new index for Sentinel-2 imagery. *Remote Sens.* **14**, 1727 (2022).
- Chen, X. et al. Estimating fire severity and carbon emissions over Australian tropical savannahs based on passive microwave satellite observations. *Int. J. Remote Sens.* **39**, 6479–6498 (2018).
- Martínez-Vilalta, J. & García-Fornier, N. Water potential regulation, stomatal behaviour and hydraulic transport under drought: deconstructing the iso/anisohydric concept. *Plant Cell Environ.* **40**, 962–976 (2017).
- Rao, K., Williams, A. P., Diffenbaugh, N. S., Yebra, M. & Konings, A. G. Plant–water sensitivity regulates wildfire vulnerability. *Nat. Ecol. Evol.* **6**, 332–339 (2022).

84. Wu, G. et al. Interannual variability of ecosystem iso/anisohydry is regulated by environmental dryness. *New Phytol.* **229**, 2562–2575 (2021).
85. Li, X. et al. Global-scale assessment and inter-comparison of recently developed/reprocessed microwave satellite vegetation optical depth products. *Remote Sens. Environ.* **253**, 112208 (2021).
86. Alonso-González, E. & Fernández-García, V. A global burn severity database from MODIS (2000–2020) (1.0.0). *Zenodo* <https://zenodo.org/record/4265209> (2020)
87. Baur, M. MartinBaur/Widespread-and-systematic-effects-of-fire-on-plant-soil-water-relations-: Fire soil plant water relations. *Zenodo* <https://doi.org/10.5281/zenodo.13768695> (2024).

Acknowledgements

M.J.B. was supported by the University of Cambridge Harding Distinguished Postgraduate Scholars Programme. A.F.A.P. was supported by funding from United Kingdom Research and Innovation Grant G123484.

Author contributions

M.J.B. designed the research in collaboration with A.D.F. and A.F.A.P., conducted the analysis and designed the figures. A.D.F. and A.F.A.P.

helped with the analysis and interpretation of results. All authors contributed to writing the paper.

Competing interests

The authors declare no competing interests.

Additional information

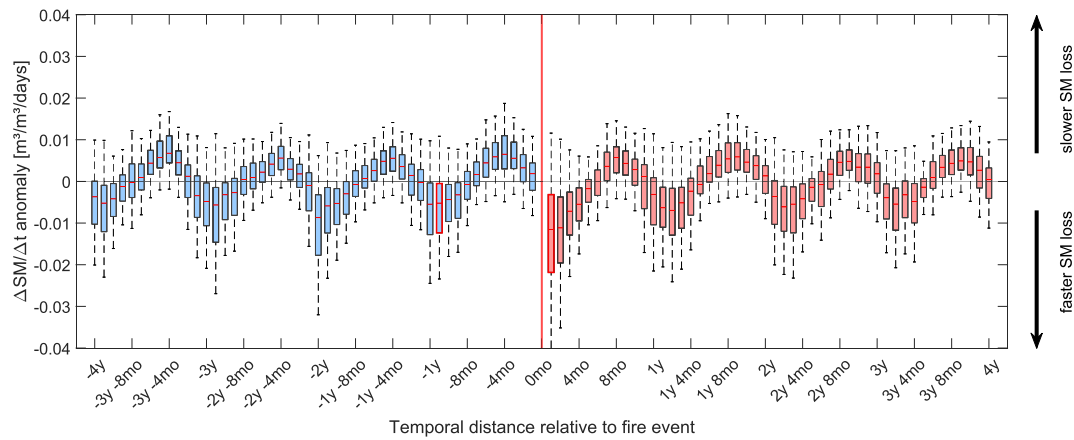
Extended data is available for this paper at <https://doi.org/10.1038/s41561-024-01563-6>.

Supplementary information The online version contains supplementary material available at <https://doi.org/10.1038/s41561-024-01563-6>.

Correspondence and requests for materials should be addressed to Martin J. Baur.

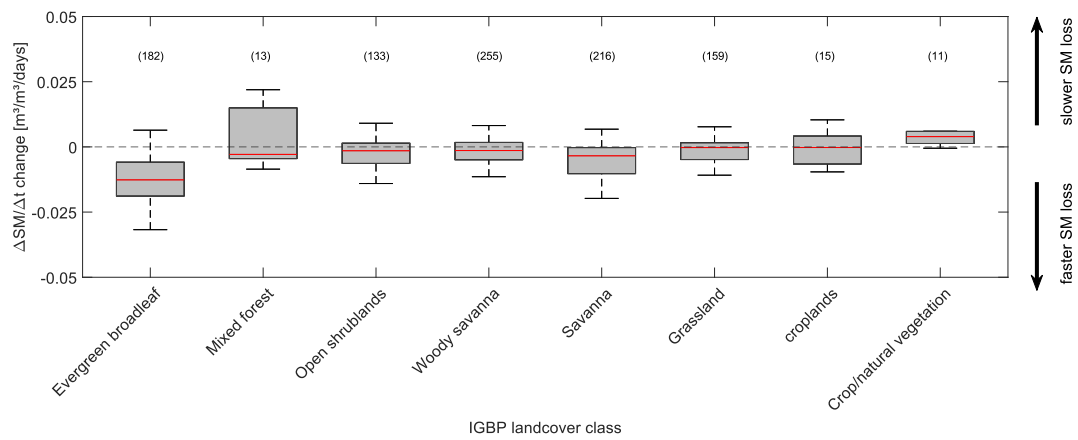
Peer review information *Nature Geoscience* thanks Rene Orth, Yan Yu and the other, anonymous, reviewer(s) for their contribution to the peer review of this work. Primary Handling Editor: Xujia Jiang, in collaboration with the *Nature Geoscience* team.

Reprints and permissions information is available at www.nature.com/reprints.



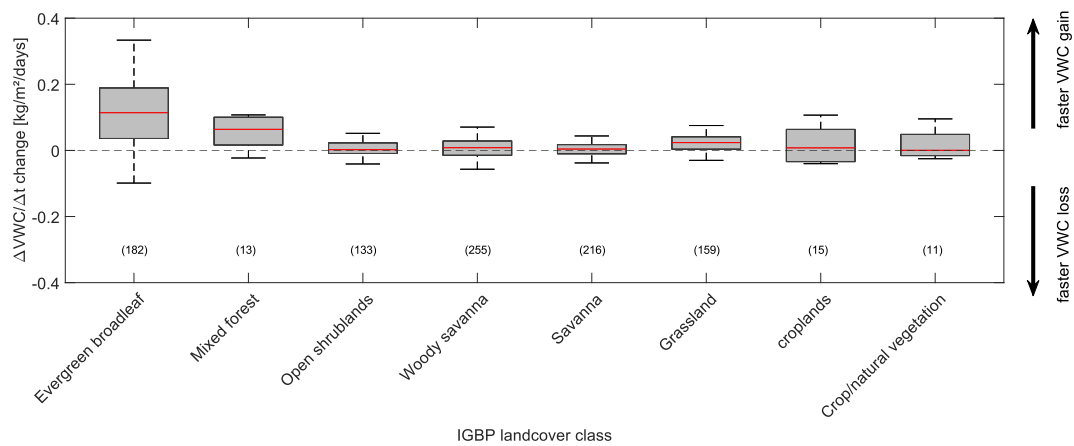
Extended Data Fig. 1 | anomalies in 30-day segments relative to the time of fire suggest that SM loss is accelerated several months after fire. Each 30-day box is computed after binning into 30 by 30 SM and VWC conditions and excluding conditions with fewer than 20 samples. Boxes indicated in red are 0-30 days post fire and the same time in the previous year, thus the data presented and

analyzed in manuscript Fig. 1. Positive anomalies suggest slower SM loss, while negative anomalies suggest accelerated loss. Boxplots display median, 25th and 75th percentile of the distribution. Whiskers include approximately 99.3% of all datapoints, and outliers are not displayed. For each box the sample size is larger than 200.



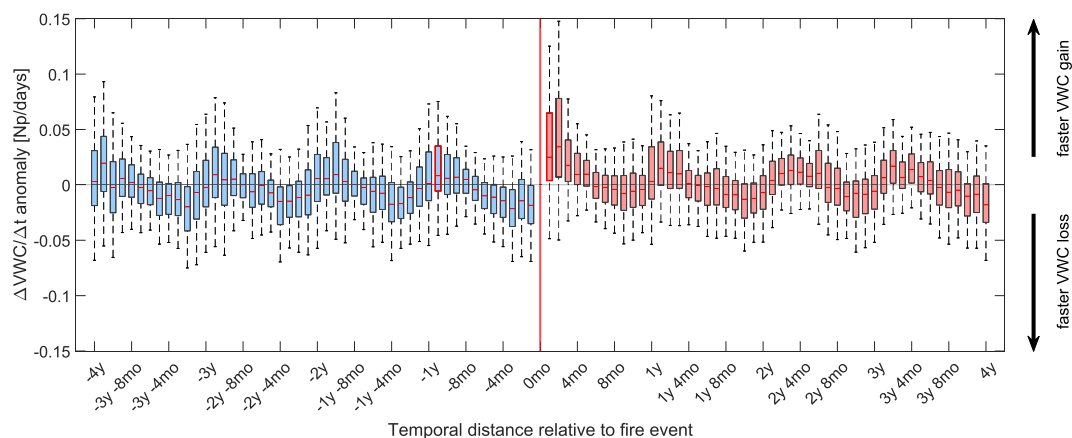
Extended Data Fig. 2 | Pre- to post-fire change of $\frac{\Delta SM}{\Delta t}$ for IGBP landcover classes. For each box underlying drydowns are binned into 30 by 30 SM and VWC conditions. For each box conditions with less than 10 samples are excluded.

Boxplots display median, 25th and 75th percentile of the distribution. Whiskers include approximately 99.3% of all datapoints, and outliers are not displayed. For each box the sample size is displayed in brackets.



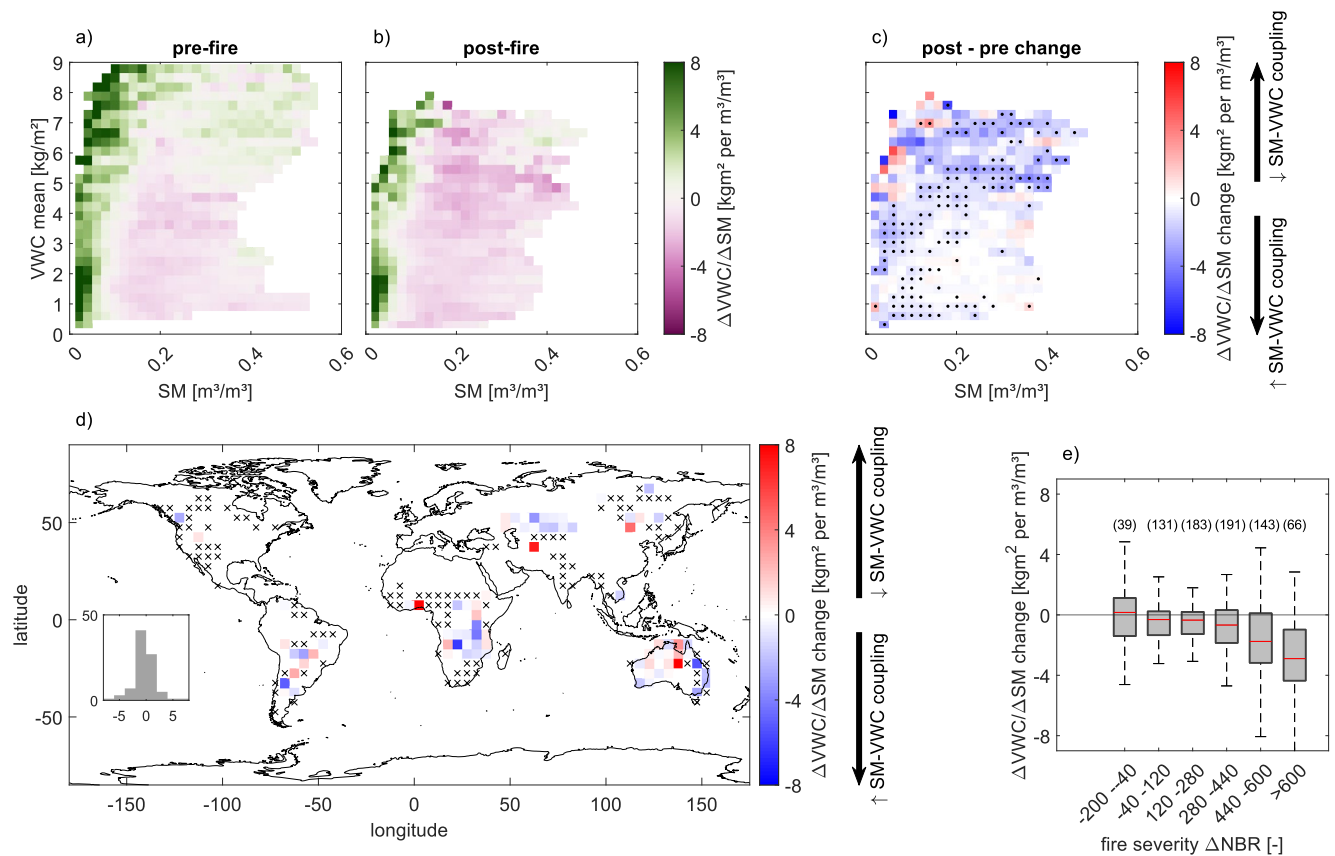
Extended Data Fig. 3 | Pre- to post-fire change of $\frac{\Delta VWC}{\Delta t}$ for IGBP landcover classes. For each box drydowns are binned into a phase space of 30 SM and VWC conditions. Conditions with less than 10 samples are excluded from the analysis.

Boxplots display median, 25th and 75th percentile of the distribution. Whiskers include approximately 99,3% of all datapoints, and outliers are not displayed. For each box the sample size is displayed in brackets.



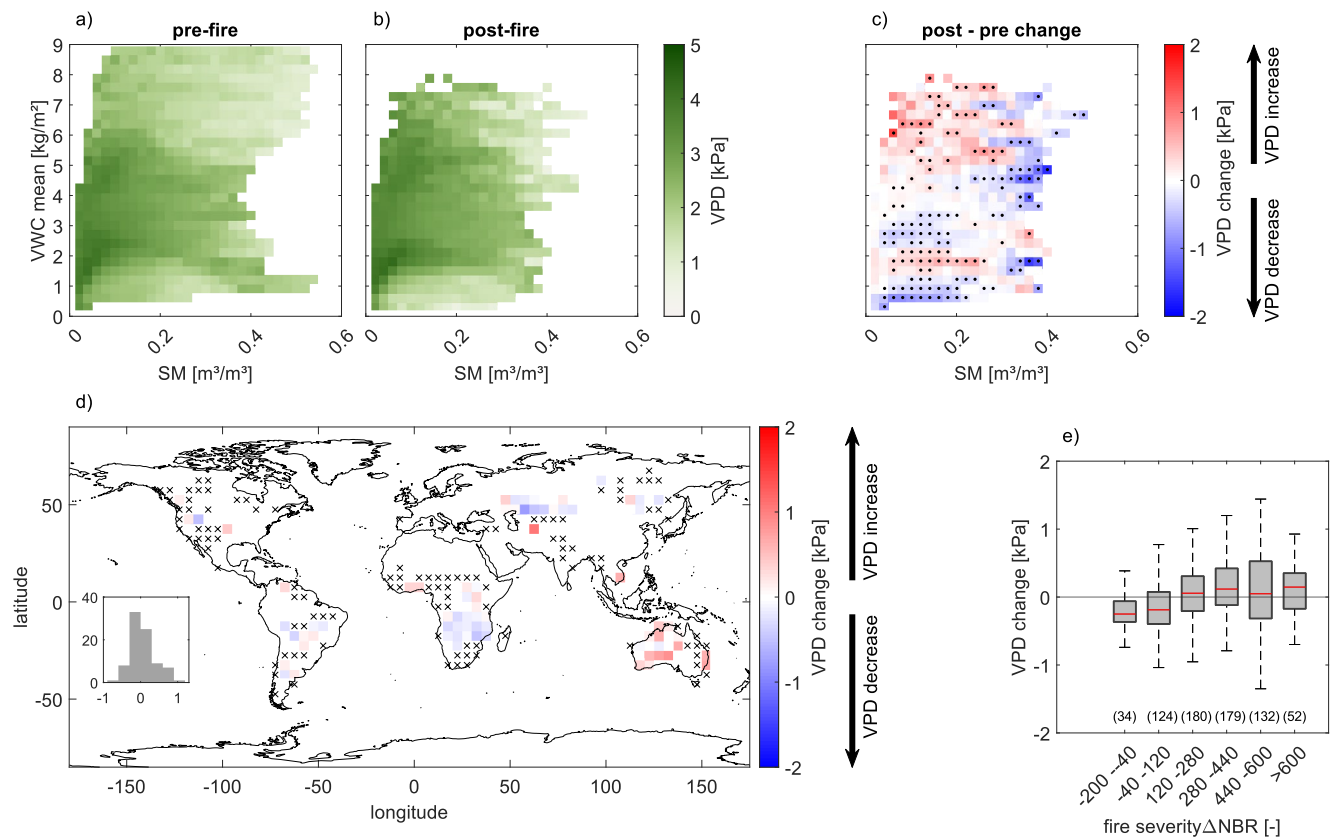
Extended Data Fig. 4 | anomalies in 30-day segments relative to the time of fire suggest persistent faster VWC gains after fire. $\frac{\Delta VWC}{\Delta t}$ Each 30-day box is computed after binning into 30 by 30 SM and VWC conditions and excluding conditions with fewer than 20 samples. Boxes indicated in red are 0–30 days post fire and the same time in the previous year, thus the data presented and analyzed

in manuscript Fig. 1. Positive anomalies suggest faster VWC gain, while negative anomalies suggest faster VWC loss. Boxplots display median, 25th and 75th percentile of the distribution. Whiskers include approximately 99.3% of all datapoints, and outliers are not displayed. For each box the sample size is larger than 200.



Extended Data Fig. 5 | Pre- and post-fire $\frac{\Delta VWC}{\Delta SM}$ suggest stronger coupling between VWC and SM post-fire. (a) Median pre-fire $\frac{\Delta VWC}{\Delta SM}$, (b) median post-fire $\frac{\Delta VWC}{\Delta SM}$ and (c) $\frac{\Delta VWC}{\Delta SM}$ post- minus pre-fire difference. We use a two-sided Wilcoxon rank sum test to determine if pre- and post-fire samples come from continuous distributions of equal mean. If this is rejected at the five percent significance level the tiles in (c) are stippled. SM and VWC conditions with fewer than 20 samples

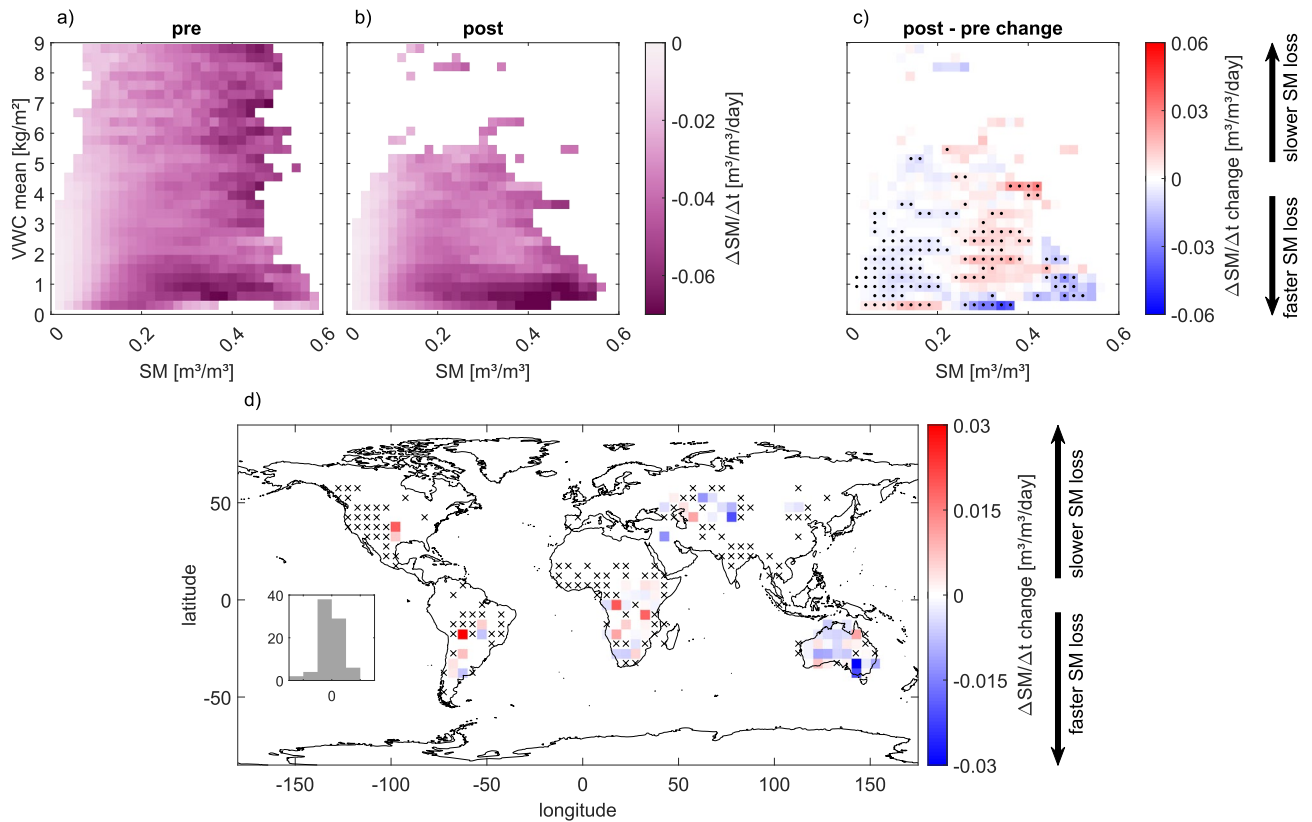
are not shown. (d) Map of the median difference between post- and pre-fire $\frac{\Delta VWC}{\Delta SM}$ binned into a 5° grid, areas with fire but insufficient sampling are indicated by crosses. (e) $\frac{\Delta VWC}{\Delta SM}$ change relative to ΔNBR fire severity. Boxplots display median, 25th and 75th percentile of the distribution. Whiskers include approximately 99.3% of all datapoints, and outliers are not displayed. For each box the sample size is displayed in brackets.



Extended Data Fig. 6 | Pre- and post-fire VPD are not substantially different across SM and VWC conditions but are modulated by fire severity.

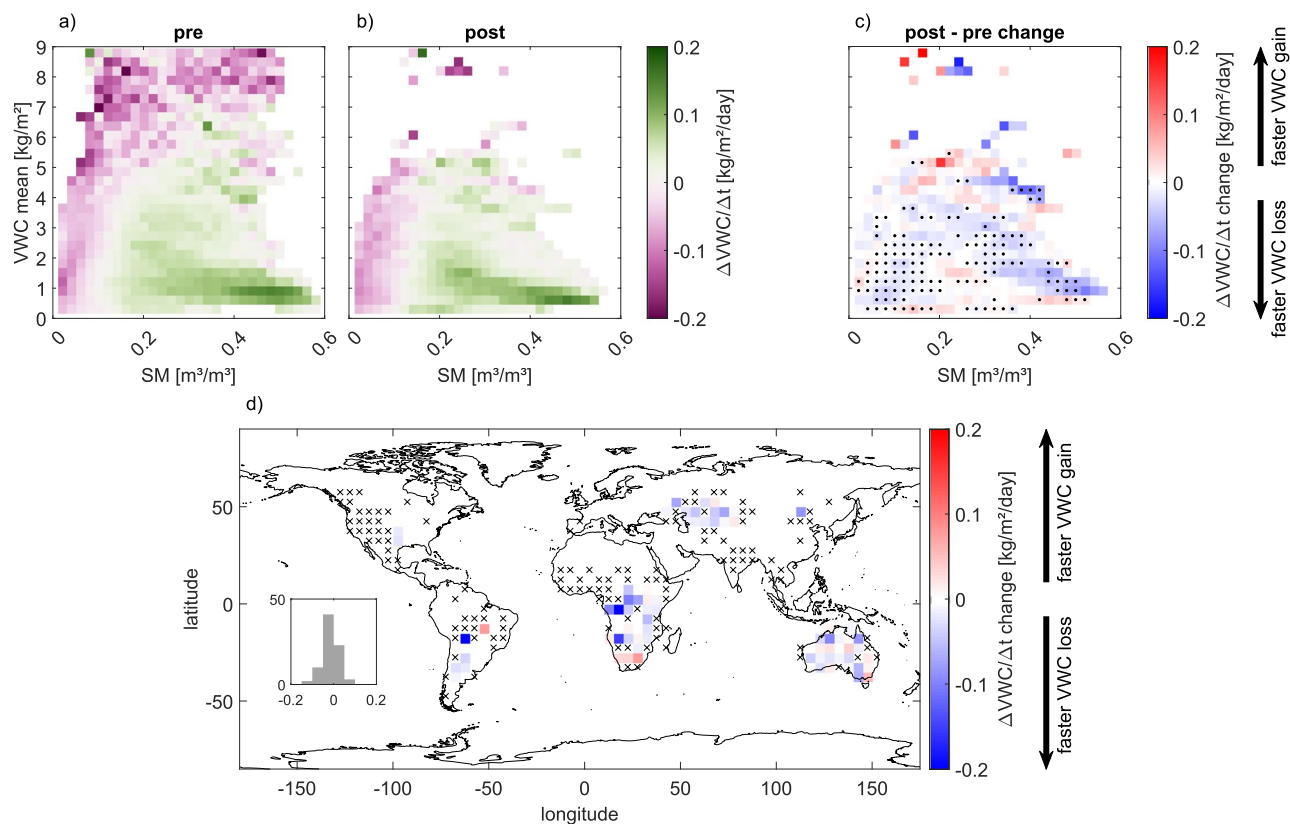
(a) Median pre-fire VPD, (b) median post-fire VPD and (c) VPD post- minus pre-fire difference. We use a two-sided Wilcoxon rank sum test to determine if pre- and post-fire samples come from continuous distributions of equal mean. If this is rejected at the five percent significance level the tiles in (c) are stippled. SM and VWC condition with fewer than 20 samples are not displayed. (d) Map of the

median difference between post- and pre-fire VPD binned into a 5° grid. Areas with detected fires but insufficient sampling are indicated by crosses. (e) VPD change relative to ΔNBR fire severity. Boxplots display median, 25th and 75th percentile of the distribution. Whiskers include approximately 99.3% of all datapoints, and outliers are not displayed. For each box the sample size is displayed in brackets.



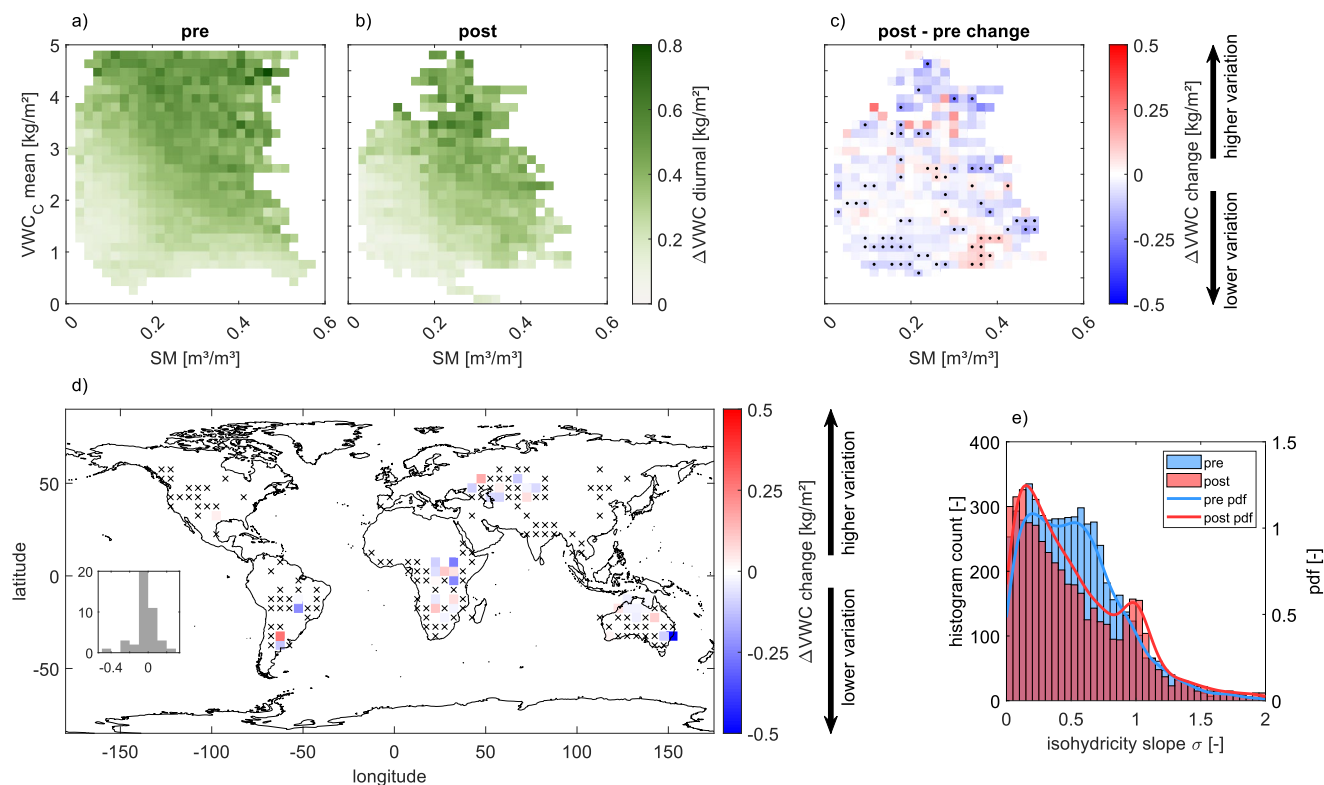
Extended Data Fig. 7 | Soil moisture rates of change $\frac{\Delta SM}{\Delta t}$ before and after point of lowest VWC for unburned reference pixels. (a) Median pre $\frac{\Delta SM}{\Delta t}$, (b) median post $\frac{\Delta SM}{\Delta t}$ and (c) $\frac{\Delta SM}{\Delta t}$ post minus pre difference. We use a two-sided Wilcoxon rank sum test to determine if pre and post samples come from

continuous distributions of equal mean. If this is rejected at a five percent significance level the tiles in (c) are stippled. SM and VWC conditions with fewer than 20 samples are not shown. (d) Map of the median difference between post and pre $\frac{\Delta SM}{\Delta t}$ binned into a 5° grid, areas with fire events but insufficient sampling are indicated by crosses.



Extended Data Fig. 8 | Vegetation water content rates of change $\frac{\Delta VWC}{\Delta t}$ before and after point of lowest VWC for unburned reference pixels. (a) Median pre $\frac{\Delta VWC}{\Delta t}$, (b) median post $\frac{\Delta VWC}{\Delta t}$ and (c) $\frac{\Delta VWC}{\Delta t}$ post minus pre difference. We use a two-sided Wilcoxon rank sum test to determine if pre and post samples come

from continuous distributions of equal mean. If this is rejected at a five percent significance level the tiles in (c) are stippled. SM and VWC conditions with fewer than 20 samples are not shown. (d) Map of the median difference between post and pre $\frac{\Delta VWC}{\Delta t}$ binned into a 5° grid, areas with fire events but insufficient sampling are indicated by crosses.



Extended Data Fig. 9 | Diurnal plant-soil water relations before and after the point of lowest VWC for unburned reference pixels. (a) Median pre $\Delta VWC_{diurnal}$, (b) median post $\Delta VWC_{diurnal}$ and (c) $\Delta VWC_{diurnal}$ post minus pre difference. We use a two-sided Wilcoxon rank sum test to determine if pre and post samples come from continuous distributions of equal mean. If this is rejected at a five percent

significance level the tiles in (c) are stippled. SM and VWC conditions with fewer than 20 samples are not shown. (d) Map of the median difference between post and pre $\Delta VWC_{diurnal}$ binned into a 5° grid, areas with fire events but insufficient sampling are indicated by crosses. (e) Pre- and post isohyricity slope σ .

Extended Data Table 1 | Linear models for $\frac{\Delta SM}{\Delta t}$ show stronger post-fire relationship between $\frac{\Delta SM}{\Delta t}$ and $\frac{\Delta VWC}{\Delta t}$, identifying plant water uptake as a potential driver of accelerated SM loss

Pre-fire			
	Estimate	Standard Error	p-value
Intercept	-0.27791	0.0022882	0
SM state	-0.6996	0.0024195	0
VWC state	-0.01686	0.0019669	1.0253e-17
$\frac{\Delta VWC}{\Delta t}$	-0.0038173	0.001939	0.048988
Adjusted R-squared = 0.371			
Post-fire			
	Estimate	Standard Error	p-value
Intercept	-0.37477	0.0029225	0
SM state	-0.74131	0.0032089	0
VWC state	0.06938	0.0030189	1.4936e-116
$\frac{\Delta VWC}{\Delta t}$	-0.1561	0.0024327	0
Adjusted R-squared = 0.426			

All variables were converted to z-scores which makes estimated coefficients comparable. P-values were calculated for the t-statistic of the two-sided hypothesis test.